2023 62nd IEEE Conference on Decision and Control (CDC)
December 13-15, 2023. Marina Bay Sands, Singapore

Formation Control of Underactuated AUVs Using the Hand Position Concept

Erling S. Lie, Josef Matouš, and Kristin Y. Pettersen

Abstract— **This paper presents an extended null-space-based behavioral algorithm for the formation control of fleets of underactuated autonomous underwater vehicles. The null-space-based controller is developed to work directly with second-order integrator systems, handling their dynamics in task space. The method is applied to the formation-path-following problem of a fleet of underactuated autonomous underwater vehicles. The nonlinear six-degrees-of-freedom model of the vehicle is transformed into a second-order integrator system using the 3D hand position output linearizing controller. The behavioral controller implements a hierarchy of path-following, formation-keeping, and collision-avoidance tasks. The closed-loop system is proven uniformly globally asymptotically stable, and the proposed method is validated through numerical simulations.**

I. Introduction

Cooperating autonomous underwater vehicles (AUVs) have become an important area of research due to their potential for performing tasks that are difficult or impossible for a single AUV to accomplish. Cooperation among AUVs can increase mission efficiency, enable the exploration of larger areas, and provide redundancy in case of system failures.

In many applications, it is desirable for a fleet of AUVs to move in formation while following a desired path. Formation path following can be achieved using a variety of control strategies. These include leader-follower approaches, where one AUV acts as a leader and the others follow its trajectory [1]–[3]. Coordinated path-following approaches use distributed control methods to achieve formation control, often based on consensus algorithms [4]–[6], while behavioral approaches focus on defining the behaviors each AUV should exhibit in order to achieve a desired formation [7], [8]. A comprehensive view of these strategies is provided in [9].

The null-space-based behavioral (NSB) approach is a popular centralized method for formation path following that has been extensively studied in the literature [10]–[14]. This strategy enables complex missions through a hierarchy that combines several simpler tasks with strict priority. In [10], a comprehensive motivation is given for the decomposition of complex path-planning and coordination in multi-agent systems into two blocks: NSB and maneuvering. The NSB block takes into account the parameters of the mission, the environment, and the state of the fleet to calculate the desired velocities for each vehicle. The desired velocities are then tracked by the maneuvering controls.

The NSB algorithm, as presented in the existing literature, is developed for single-integrator systems [10]–[12]. Herein, we extend the NSB method to vehicles with double-integrator dynamics and propose an algorithm that uses the second-order closed-loop inverse kinematics (SOCLIK) equation to control the task variables through desired acceleration. The procedure is inspired by robotic manipulators, where second-order methods are more common, due to the inherent second-order dynamics of mechanical systems [15], [16]. Although existing NSB methods are developed for first-order systems, AUV dynamics are inherently second-order. Therefore, any first-order solution is necessarily perturbed by the dynamics of the maneuvering controller. In contrast, our formulation handles the second-order dynamics directly in the task space as interpretable spring-damper systems.

We apply the proposed NSB method to a fleet of AUVs. AUVs are underactuated systems with inherently nonlinear dynamics. What enables us to still use the proposed NSB method, developed for vehicles with linear double integrator dynamics, is the use of the hand position input-output linearization method, [17]–[20], for maneuvering control. Specifically, we apply the 3D hand position method proposed in [20], which transforms the underactuated six-degrees-of-freedom AUV model into a double-integrator system. Subsequently, through the design of specific path-following, formation-keeping, and collision-avoidance tasks, the fleet is controlled to follow a preplanned path in formation while avoiding collisions both within the fleet and with external obstacles. The stability of the system is proved, and its effectiveness is verified in simulations. Because our reformulated NSB method works directly with the second-order system given by the hand position controller, there is no need to transform desired velocities or accelerations into surge and orientation references, as has been done in previous works. This reduces one level of complexity in the controller design.

The paper is organized as follows. Section II presents the extended NSB algorithm which is applicable for general double-integrator systems. Section III presents a case study of this NSB algorithm applied to a fleet of AUVs. Section IV presents conclusions and future work.

II. The NSB Algorithm for Double Integrators

The NSB method enables the creation of multiple tasks in a hierarchical manner, ensuring that low-priority tasks do not interfere with high-priority ones. In this section, we extend this method to second-order systems. This modified NSB

This work was partly supported by the Research Council of Norway through project No. 302435 and the Centres of Excellence funding scheme, project No. 223254.

E. S. Lie, J. Matouš, and K. Y. Pettersen are with the Department of Engineering Cybernetics, Norwegian University of Science and Technology (NTNU), Trondheim, Norway. {erling.s.lie, josef.matous, kristin.y.pettersen}@ntnu.no

algorithm provides the acceleration input $\boldsymbol{\mu}$ to the following double-integrator system

$$\dot{\mathbf{p}} = \mathbf{v}, \tag{1a}$$
$$\dot{\mathbf{v}} = \boldsymbol{\mu}. \tag{1b}$$

In the NSB algorithm, the control goals are expressed as a series of tasks. Each task is defined using a task variable $\boldsymbol{\sigma}_i \in \mathbb{R}^{m_i}$, as a function of $\mathbf{p}$

$$\boldsymbol{\sigma}_i = \mathbf{f}_i(\mathbf{p}). \tag{2}$$

The first and second time-derivatives of $\boldsymbol{\sigma}_i$ are

$$\dot{\boldsymbol{\sigma}}_i = \mathbf{J}_i \mathbf{v}, \tag{3a}$$
$$\ddot{\boldsymbol{\sigma}}_i = \mathbf{J}_i \dot{\mathbf{v}} + \dot{\mathbf{J}}_i \mathbf{v}, \tag{3b}$$

where $\mathbf{J}_i = \partial \mathbf{f}_i / \partial \mathbf{p}$ is the task Jacobian.

Let $\ddot{\boldsymbol{\sigma}}_i^*$ be the desired behavior of the task. Then, the smallest control input (in terms of Euclidean norm) that achieves this behavior is given by

$$\dot{\mathbf{v}}_i = \mathbf{J}_i^\dagger \left(\ddot{\boldsymbol{\sigma}}_i^* - \dot{\mathbf{J}}_i \mathbf{v} \right), \tag{4}$$

where $\mathbf{J}_i^\dagger$ is the pseudoinverse of $\mathbf{J}_i$.

Now, let us consider a case when the task variable should track some predefined desired value $\boldsymbol{\sigma}_{d,i}$. In the standard NSB algorithm, which was developed for single-integrator systems

$$\dot{\mathbf{p}} = \mathbf{v}, \tag{5}$$

the control input $\mathbf{v}_i$ for tracking the desired value is obtained through the so-called *closed-loop inverse kinematics* (CLIK) equation [21]

$$\mathbf{v}_i = \mathbf{J}_i^\dagger \dot{\boldsymbol{\sigma}}_i^*, \qquad \dot{\boldsymbol{\sigma}}_i^* = \dot{\boldsymbol{\sigma}}_{d,i} - \boldsymbol{\Lambda}_i \tilde{\boldsymbol{\sigma}}_i, \tag{6}$$

where $\tilde{\boldsymbol{\sigma}}_i = \boldsymbol{\sigma}_i - \boldsymbol{\sigma}_{d,i}$, and $\boldsymbol{\Lambda}_i$ is a positive definite gain matrix.

In second-order differential control, we propose a similar *second-order closed-loop inverse kinematics* (SOCLIK) equation inspired by robotic manipulators [22]. The SOCLIK solution for tracking a desired value is given by

$$\ddot{\boldsymbol{\sigma}}_i^* = \ddot{\boldsymbol{\sigma}}_{d,i} - \boldsymbol{\Lambda}_{p,i} \tilde{\boldsymbol{\sigma}}_i - \boldsymbol{\Lambda}_{d,i} \dot{\tilde{\boldsymbol{\sigma}}}_i, \tag{7}$$

where $\dot{\tilde{\boldsymbol{\sigma}}}_i = \dot{\boldsymbol{\sigma}}_i - \dot{\boldsymbol{\sigma}}_{d,i}$, and $\boldsymbol{\Lambda}_{p,i}$ and $\boldsymbol{\Lambda}_{d,i}$ are positive definite gain matrices.

In the standard NSB algorithm, there exists a subspace of velocities that do not conflict with a given task. Similarly, in second-order systems, there exists a subspace of non-conflicting accelerations. If we denote $\dot{\mathbf{v}}_1$ as the SOCLIK solution to the highest priority task, there exists an acceleration $\dot{\mathbf{v}}_{NSB}$ that also satisfies this task:

$$\dot{\mathbf{v}}_{NSB} = \dot{\mathbf{v}}_1 + \mathbf{N}_1 \dot{\mathbf{v}}_2, \tag{8}$$

where $\mathbf{N}_1 = \mathbb{I} - \mathbf{J}_1^\dagger \mathbf{J}_1$ is the null space projector of task 1, and $\dot{\mathbf{v}}_2$ is some additional desired acceleration resulting from other tasks. The relation can be generalized to obtain a solution for N tasks:

$$\dot{\mathbf{v}}_{NSB} = \sum_{i=1}^{N} \bar{\mathbf{N}}_i \dot{\mathbf{v}}_i, \tag{9}$$

where $\bar{\mathbf{N}}_i$ is the null space projector of the augmented Jacobian of all higher priority tasks $\bar{\mathbf{J}}_i = [\mathbf{J}_1^{\mathrm{T}} \dots \mathbf{J}_{i-1}^{\mathrm{T}}]^{\mathrm{T}}$. With this choice of acceleration, the highest priority task is always fulfilled, whereas the lower priority tasks are fulfilled as well as possible in the subspace that does not conflict with the higher-priority tasks. The commanded acceleration $\boldsymbol{\mu}$ is then given by the NSB acceleration

$$\boldsymbol{\mu} = \dot{\mathbf{v}}_{NSB}. \tag{10}$$

A. Stability Analysis

In this section, we investigate the stability of an NSB algorithm consisting of two tasks. The proof is based on [23], but extended to a double integrator system. First, let us present the concepts of task independence and orthogonality.

Definition 1: Let $\mathbf{J}_1$ and $\mathbf{J}_2$ denote the Jacobians of tasks 1 and 2. These two tasks are *orthogonal* if

$$\mathbf{J}_1 \mathbf{J}_2^\dagger = \mathbf{O}, \tag{11}$$

where $\mathbf{O}$ is a matrix of zeros. The tasks are *independent* if

$$\rho\left(\mathbf{J}_1^{\mathrm{T}}\right) + \rho\left(\mathbf{J}_2^{\mathrm{T}}\right) = \rho\left(\left[\mathbf{J}_1^{\mathrm{T}}\, \mathbf{J}_2^{\mathrm{T}}\right]\right), \tag{12}$$

where $\rho(\cdot)$ is the rank of the matrix.

Theorem 1: Consider two independent and orthogonal tasks 1 and 2. Let $\tilde{\mathbf{X}}^{\mathrm{T}} = \left[\tilde{\boldsymbol{\sigma}}_1^{\mathrm{T}}, \tilde{\boldsymbol{\sigma}}_2^{\mathrm{T}}, \dot{\tilde{\boldsymbol{\sigma}}}_1^{\mathrm{T}}, \dot{\tilde{\boldsymbol{\sigma}}}_2^{\mathrm{T}}\right]$ denote the stacked error vector.

The control input defined in (8) ensures that $\tilde{\mathbf{X}} = \mathbf{0}$ is a globally exponentially stable equilibrium point.

Proof: First, let us find the closed-loop expressions for $\ddot{\tilde{\boldsymbol{\sigma}}}_1$ and $\ddot{\tilde{\boldsymbol{\sigma}}}_2$, from (3b), (8), and (10):

$$\ddot{\tilde{\boldsymbol{\sigma}}}_1 = \mathbf{J}_1 \dot{\mathbf{v}}_1 + \mathbf{J}_1 \mathbf{N}_1 \dot{\mathbf{v}}_2 + \dot{\mathbf{J}}_1 \mathbf{v} - \ddot{\boldsymbol{\sigma}}_{d,1}, \tag{13a}$$
$$\ddot{\tilde{\boldsymbol{\sigma}}}_2 = \mathbf{J}_2 \dot{\mathbf{v}}_1 + \mathbf{J}_2 \mathbf{N}_1 \dot{\mathbf{v}}_2 + \dot{\mathbf{J}}_2 \mathbf{v} - \ddot{\boldsymbol{\sigma}}_{d,2}, \tag{13b}$$

Note that thanks to the independence and orthogonality assumptions, it follows that $\mathbf{J}_2 \mathbf{N}_1 \mathbf{J}_2^\dagger = \mathbb{I}$. Consequently, substituting (4) into (13) and using (3), the time-derivative of $\tilde{\mathbf{X}}$ is given by

$$\dot{\tilde{\mathbf{X}}} = \mathbf{M} \tilde{\mathbf{X}}, \tag{14}$$

where

$$\mathbf{M} = \begin{bmatrix} \mathbf{O} & \mathbf{O} & \mathbb{I} & \mathbf{O} \\ \mathbf{O} & \mathbf{O} & \mathbf{O} & \mathbb{I} \\ -\boldsymbol{\Lambda}_{p,1} & \mathbf{O} & -\boldsymbol{\Lambda}_{d,1} & \mathbf{O} \\ \mathbf{O} & -\boldsymbol{\Lambda}_{p,2} & \mathbf{O} & -\boldsymbol{\Lambda}_{d,2} \end{bmatrix}. \tag{15}$$

Since the gain matrices are positive definite by design, the matrix $\mathbf{M}$ is Hurwitz, and the closed-loop system is globally exponentially stable (GES). ■

III. Case Study: Formation Path Following of AUVs

The following sections present a case study of the proposed NSB algorithm applied to a fleet of underactuated

AUVs equipped with the hand-position-based controller from [20]. The control objective of the fleet is to follow a predefined path while keeping formation and avoiding obstacles.

The vehicle model under the hand position controller is presented in Section III-A and the formation path following problem is formulated in Section III-B. The NSB tasks are detailed in Section III-C, Section III-D details the obstacle avoidance method, Section III-E analyzes the stability properites, and Section III-F presents a simulation study.

A. AUV model

We consider a six degree-of-freedom model of an AUV exposed to an unknown constant irrotational ocean current. The AUV's position, attitude, translational and rotational velocities are denoted by $\boldsymbol{\eta} \in \mathbb{R}^3$, $\mathbf{R} \in SO(3)$, $\boldsymbol{\nu} \in \mathbb{R}^3$, and $\boldsymbol{\omega} \in \mathbb{R}^3$, respectively. The relative linear velocity between the AUV and current is $\boldsymbol{\nu}_r = \boldsymbol{\nu} - \mathbf{R}^{\mathrm{T}}\mathbf{v}_c$, and the concatenated velocity vector is $\boldsymbol{\zeta}_r^{\mathrm{T}} = [\boldsymbol{\nu}_r^{\mathrm{T}}, \boldsymbol{\omega}^{\mathrm{T}}]$.

The 3D hand position transformation consists of the following change of coordinates

$$\mathbf{x}_1 = \boldsymbol{\eta} + \mathbf{R}\mathbf{L}, \tag{16a}$$

$$\mathbf{x}_2 = \mathbf{R}\boldsymbol{\nu}_r + \mathbf{R}(\boldsymbol{\omega} \times \mathbf{L}), \tag{16b}$$

where $\mathbf{L} = [h, 0, 0]^{\mathrm{T}}$, and $h > 0$ is the *hand length*.

The transformed model of the AUV is then given by

$$\dot{\mathbf{x}}_1 = \mathbf{x}_2 + \mathbf{v}_c, \tag{17a}$$

$$\dot{\mathbf{x}}_2 = \boldsymbol{\mu}, \tag{17b}$$

$$\dot{\mathbf{R}} = \mathbf{R}\mathbf{S}(\boldsymbol{\omega}), \tag{17c}$$

$$\begin{aligned}\dot{\boldsymbol{\omega}} = \bar{\mathbf{L}} \times \left(\mathbf{R}^{\mathrm{T}}\boldsymbol{\mu} + \mathcal{D}_{\boldsymbol{\nu}}(\boldsymbol{\zeta}_r) + \mathcal{C}_{\boldsymbol{\nu}}(\boldsymbol{\zeta}_r) - \boldsymbol{\omega} \times \mathbf{R}^{\mathrm{T}}\mathbf{x}_2\right) \\ - \left(\bar{\mathbf{L}}\mathbf{L}^{\mathrm{T}}\right)\left(\mathcal{D}_{\boldsymbol{\omega}}(\boldsymbol{\zeta}_r) + \mathbf{M}'_{22}(W\mathbf{z}_{gb}\mathbf{e}_3 \times \mathbf{R}^{\mathrm{T}}\mathbf{e}_3)\right),\end{aligned} \tag{17d}$$

where $\boldsymbol{\mu}$ is the transformed control input. The definitions of the vectors and matrices $\mathbf{L}$, $\bar{\mathbf{L}}$, $\mathbf{M}'_{22}$, $\mathbf{z}_{gb}$, $\mathbf{e}_3$, $\mathcal{D}_{\boldsymbol{\nu}}$, $\mathcal{D}_{\boldsymbol{\omega}}$ and $\mathcal{C}_{\boldsymbol{\nu}}$ are given in [20].

Note that through the 3D hand position concept, the underactuated and highly nonlinear AUV model is now transformed to an input-output feedback linearized form, where the external part of the system, $\mathbf{x}_1$ and $\mathbf{x}_2$, denotes the hand position and velocity of the vehicle, while the internal part of the system is given by $\mathbf{R}$ and $\boldsymbol{\omega}$.

B. Formation Path Following

We consider a fleet of n AUVs following a path in the inertial coordinate frame given by a smooth function $\mathbf{p}_p : \mathbb{R} \mapsto \mathbb{R}^3$, and define the stacked position and velocity vectors $\mathbf{p} = [\mathbf{x}_{1,1}^{\mathrm{T}}, \ldots, \mathbf{x}_{1,n}^{\mathrm{T}}]^{\mathrm{T}}$ and $\mathbf{v} = [\mathbf{x}_{2,1}^{\mathrm{T}}, \ldots, \mathbf{x}_{2,n}^{\mathrm{T}}]^{\mathrm{T}}$, respectively. We also define the stacked ocean current vector $\mathbf{V}_c = \mathbf{1}_{n,1} \otimes \mathbf{v}_c$, where $\mathbf{1}_{n,1}$ is an n-dimensional vector of ones, and $\otimes$ is the Kronecker product. We will in the following denote the position of a single AUV by $\mathbf{p}_i := \mathbf{x}_{1,i}$ and its velocity relative to the ocean current by $\mathbf{v}_i := \mathbf{x}_{2,i}$.

The path function is assumed to be $\mathcal{C}^\infty$ and regular, meaning that the function is continuously differentiable and the partial derivative with respect to ξ satisfies $\left\| \frac{\partial \mathbf{p}_p(\xi)}{\partial \xi} \right\| \neq 0$.

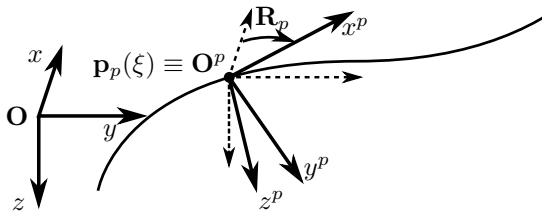

Fig. 1. Definition of the path angles and path-tangential coordinate frame. $\mathbf{O}$ denotes the origin of the inertial coordinate frame, $\mathbf{O}^p$ denotes the origin of the path-tangential frame.

For every point $\mathbf{p}_p(\xi)$, there exists a path-tangential coordinate-frame with a corresponding rotation matrix $\mathbf{R}_p$ (see Fig. 1). The path-following error $\mathbf{p}_b^p$ is defined in terms of the barycenter of the fleet in the path-tangential coordinate frame:

$$\mathbf{p}_b^p = \mathbf{R}_p^{\mathrm{T}}\left(\mathbf{p}_b - \mathbf{p}_p(\xi)\right), \quad \mathbf{p}_b = \frac{1}{n}\sum_{i=1}^{n}\mathbf{p}_i. \tag{18}$$

The formation is defined in the formation-centered coordinate frame, centered at $\mathbf{p}_b$ with the same orientation as the path-tangential frame (see Fig. 2). The position of vehicle i in the formation-centered frame is given by

$$\mathbf{p}_i^f = \mathbf{R}_p^{\mathrm{T}}\left(\mathbf{p}_i - \mathbf{p}_b\right), \tag{19}$$

and the desired positions are given by $\mathbf{p}_{f,1}^f, \ldots, \mathbf{p}_{f,n}^f$.

C. NSB Controller

We let the control system consist of three tasks in decreasing order of priority: inter-vehicle collision avoidance, formation keeping, and path following. The following sections will detail the chosen task variables and SOCLIK solution for each task.

1) Inter-vehicle collision avoidance: The highest-priority task is inter-vehicle collision avoidance (COLAV). This task is active only when two vehicles are closer than an activation distance d_{COLAV}. The task variable is given by a stacked vector $\boldsymbol{\sigma}_1 = [\sigma_{1,1}^{\mathrm{T}}, \ldots, \sigma_{1,l}^{\mathrm{T}}]^{\mathrm{T}}$ of relative distances between vehicles closer than the activation distance:

$$\begin{aligned}\sigma_{1,k} = \|\mathbf{p}_i - \mathbf{p}_j\|, \quad \forall i, j \in 1, \ldots, n : j > i, \\ \|\mathbf{p}_i - \mathbf{p}_j\| < d_{COLAV}.\end{aligned} \tag{20}$$

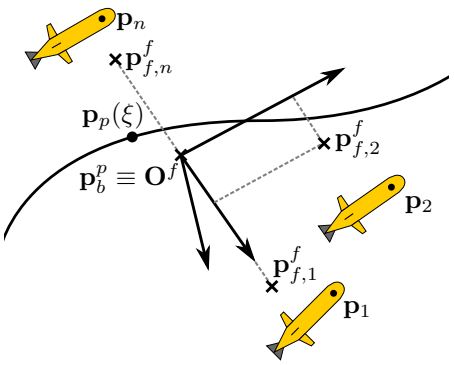

Fig. 2. Definition of the formation. $\mathbf{O}^f$ denotes the origin of the formation-centered coordinate frame.

The dimension of $\boldsymbol{\sigma}_1$ varies depending on the number of vehicles that are within the activation distance, and it is empty if there is no risk of collision. The desired values of the task are given by

$$\boldsymbol{\sigma}_{d,1} = d_{COLAV}\mathbf{1}_l, \tag{21}$$

which ensures that the vehicles recover the safe distance d_{COLAV} whenever the threshold is violated. We note that $\ddot{\boldsymbol{\sigma}}_{d,1} = \dot{\boldsymbol{\sigma}}_{d,1} = 0$.

The task Jacobian is given by the stacked partial derivatives for each active collision

$$\mathbf{J}_1 = \begin{bmatrix} \left(\frac{\partial \sigma_{1,1}}{\partial \mathbf{p}}\right)^{\mathrm{T}}, \ldots, \left(\frac{\partial \sigma_{1,l}}{\partial \mathbf{p}}\right)^{\mathrm{T}} \end{bmatrix}^{\mathrm{T}}, \tag{22a}$$

$$\frac{\partial \sigma_{1,k}}{\partial \mathbf{p}_i} = \frac{(\mathbf{p}_i - \mathbf{p}_j)^{\mathrm{T}}}{\|\mathbf{p}_i - \mathbf{p}_j\|}, \; \frac{\partial \sigma_{1,k}}{\partial \mathbf{p}_j} = -\frac{(\mathbf{p}_i - \mathbf{p}_j)^{\mathrm{T}}}{\|\mathbf{p}_i - \mathbf{p}_j\|}. \tag{22b}$$

The resulting SOCLIK equation for the task is

$$\dot{\mathbf{v}}_1 = -\mathbf{J}_1^{\dagger}\big(\boldsymbol{\Lambda}_{p,1}\tilde{\boldsymbol{\sigma}}_1 + \boldsymbol{\Lambda}_{d,1}\dot{\boldsymbol{\sigma}}_1 + \dot{\mathbf{J}}_1(\mathbf{v} + \mathbf{V}_c)\big), \tag{23}$$

with $\dot{\boldsymbol{\sigma}}_1 = \mathbf{J}_1(\mathbf{v} + \mathbf{V}_c)$. Note that due to the structure of the task Jacobian, it follows that $\mathbf{J}_1\mathbf{V}_c = \dot{\mathbf{J}}_1\mathbf{V}_c = \mathbf{0}$. Consequently, $\dot{\mathbf{v}}_1$ is independent of the ocean current velocity.

2) Formation-Keeping Task: The formation-keeping task moves the vehicles into a predefined formation in the formation-centered frame. The task variable is given by

$$\boldsymbol{\sigma}_2 = \left[\boldsymbol{\sigma}_{2,1}^{\mathrm{T}}, ..., \boldsymbol{\sigma}_{2,n-1}^{\mathrm{T}}\right]^{\mathrm{T}}, \quad \boldsymbol{\sigma}_{2,i} = \mathbf{p}_i - \mathbf{p}_b. \tag{24}$$

The desired values are

$$\boldsymbol{\sigma}_{d,2} = [\left(\mathbf{R}_p\mathbf{p}_{f,1}^f\right)^{\mathrm{T}}, ..., \left(\mathbf{R}_p\mathbf{p}_{f,n-1}^f\right)^{\mathrm{T}}]^{\mathrm{T}}. \tag{25}$$

There is one fewer task than AUVs to avoid singularities, as the last AUV's position is implied by the fact that $\sum_{i=1}^{n}\mathbf{p}_{f,1}^f = \mathbf{0}$. The Jacobian is given by

$$\mathbf{J}_2 = \left(\begin{bmatrix}\mathbb{I}_{n-1} & \mathbf{0}_{n-1,1}\end{bmatrix} - \frac{\mathbf{1}_{n-1,n}}{N}\right) \otimes \mathbb{I}_3. \tag{26}$$

Because $\dot{\mathbf{J}}_2 = \mathbf{0}$, the SOCLIK equation reduces to

$$\dot{\mathbf{v}}_2 = \mathbf{J}_2^{\dagger}\big(\ddot{\boldsymbol{\sigma}}_{d,2} - \boldsymbol{\Lambda}_{p,2}\tilde{\boldsymbol{\sigma}}_2 - \boldsymbol{\Lambda}_{d,2}\dot{\tilde{\boldsymbol{\sigma}}}_2\big). \tag{27}$$

The nominal task acceleration (27) may saturate the actuators if the formation error is large. The NSB controller may also lead to a loss of controllability if the formation-keeping velocities exactly cancel out the path-following velocities. Therefore, we introduce the saturated task acceleration

$$\dot{\mathbf{v}}_2 = \mathbf{J}_2^{\dagger}\big(\ddot{\boldsymbol{\sigma}}_{d,2} - v_{2_{\max}}\mathrm{sat}\big(\boldsymbol{\Lambda}_{p,2}\tilde{\boldsymbol{\sigma}}_2\big) - \boldsymbol{\Lambda}_{d,2}\dot{\tilde{\boldsymbol{\sigma}}}_2\big), \tag{28}$$

where $v_{2_{\max}}$ is a positive constant and sat is a saturation function given by

$$\mathrm{sat}\big(\mathbf{x}\big) = \mathbf{x}\frac{\tanh\|\mathbf{x}\|}{\|\mathbf{x}\|}. \tag{29}$$

With the saturated task acceleration, we further require that the product of the gain matrices $\boldsymbol{\Lambda}_{p,2}\boldsymbol{\Lambda}_{d,2}$ is symmetric positive definite.

Like the inter-vehicle collision avoidance task, this task is independent of the ocean current.

3) Path-Following Task: The path following task concerns moving the barycenter along the predefined path. Moreover, we want the formation to move at a constant, positive, desired path-following speed $U_{LOS} > 0$.

The path-following task variable is given by the barycenter $\boldsymbol{\sigma_3} = \mathbf{p}_b$, with $\mathbf{p}_b$ given by (18). The corresponding task Jacobian and its pseudoinverse are given by

$$\mathbf{J}_3 = \frac{1}{n}\mathbf{1}_{1,n} \otimes \mathbb{I}_3, \qquad \mathbf{J}_3^{\dagger} = \mathbf{1}_{n,1} \otimes \mathbb{I}_3. \tag{30}$$

Inserting the pseudoinverse into (4), the same acceleration is applied to all vehicles. Furthermore, the Jacobians of the formation-keeping and path-following tasks satisfy the definitions of independence and orthogonality (11), (12).

To achieve the path-following task, we define the following desired task behavior:

$$\ddot{\boldsymbol{\sigma}}_3^* = \dot{\mathbf{v}}_{LOS,d} + \boldsymbol{\Lambda}_{p,3}(\mathbf{v}_{LOS,d} - \dot{\boldsymbol{\sigma}}_3) + \boldsymbol{\Lambda}_{i,3}(\mathbf{p}_v - \boldsymbol{\sigma}_3), \tag{31}$$

where $\mathbf{v}_{LOS,d}$ is the desired velocity given by the line-of-sight (LOS) guidance law from [12]. Let x_b^p, y_b^p, and z_b^p be the components of the path-following error $\mathbf{p}_b^p$. Then, the LOS velocity is given by

$$\mathbf{v}_{LOS,d} = \mathbf{R}_p\left[\Delta(\mathbf{p}_b^p), -y_b^p, -z_b^p\right]^{\mathrm{T}}\frac{U_{LOS}}{D}. \tag{32}$$

In addition, we use a virtual integral state $\mathbf{p}_v$ to eliminate the tracking error caused by the ocean current

$$\dot{\mathbf{p}}_v = \mathbf{v}_{LOS,d}. \tag{33}$$

As we mentioned previously, other tasks are not affected by the ocean current. Therefore, we only need to counteract the ocean current in this task.

The term $\Delta(\mathbf{p}_b^p)$ is an error-dependent look-ahead distance

$$\Delta(\mathbf{p}_b^p) = \sqrt{\Delta_0^2 + (x_b^p)^2 + (y_b^p)^2 + (z_b^p)^2}, \tag{34}$$

where Δ_0 is a positive constant, and

$$D = \sqrt{\Delta(\cdot)^2 + (y_b^p)^2 + (z_b^p)^2} \tag{35}$$

is a normalization term.

Lemma 1: Let $\boldsymbol{\Lambda}_{p,3}$ and $\boldsymbol{\Lambda}_{i,3}$ be two symmetric positive definite matrices. The relative barycenter velocity $\mathbf{v}_b$ converges exponentially to the relative LOS velocity $\mathbf{v}_{LOS,d} - \mathbf{v}_c$ under the controller (9), (10), with the path-following task-acceleration given by (31).

Proof: We define the following error variables

$$\tilde{\mathbf{p}} = \mathbf{p}_b - \mathbf{p}_v - \boldsymbol{\Lambda}_{i,3}^{-1}\boldsymbol{\Lambda}_{p,3}\mathbf{v}_c, \tag{36a}$$

$$\tilde{\mathbf{v}} = \mathbf{v}_b - \left(\mathbf{v}_{LOS,d} - \mathbf{v}_c\right), \tag{36b}$$

which have the following linear dynamics

$$\begin{bmatrix}\dot{\tilde{\mathbf{p}}} \\ \dot{\tilde{\mathbf{v}}}\end{bmatrix} = \begin{bmatrix}\mathbf{0} & \mathbb{I} \\ -\boldsymbol{\Lambda}_{i,3} & -\boldsymbol{\Lambda}_{p,3}\end{bmatrix}\begin{bmatrix}\tilde{\mathbf{p}} \\ \tilde{\mathbf{v}}\end{bmatrix}. \tag{37}$$

This system is GES, meaning that $\tilde{\mathbf{v}}$ exponentially converges to zero. Consequently, $\mathbf{v}_b$ converges to $\mathbf{v}_{LOS,d} - \mathbf{v}_c$. ■

The desired acceleration for the path-following is then

given by

$$\dot{\mathbf{v}}_3 = \mathbf{J}_3^{\dagger}\ddot{\boldsymbol{\sigma}}_3^{*} = \mathbf{1}_{n,1} \otimes \ddot{\boldsymbol{\sigma}}_3^{*}. \tag{38}$$

Like in [12], the update of the path-parameter ξ is used as an extra degree of freedom to guarantee along-track stability

$$\dot{\xi} = U_{LOS} \left\| \frac{\partial \mathbf{p}_p(\xi)}{\partial \xi} \right\|^{-1} \left(\frac{\Delta(\mathbf{p}_b^p)}{D} + k_\xi \frac{x_b^p}{\sqrt{1+(x_b^p)^2}} \right). \tag{39}$$

This choice ensures that the desired LOS velocity (32) guarantees USGES of the path-following task, which we will rely on in the stability proof presented in Section III-E.

D. Obstacle avoidance

We implement an obstacle avoidance method that enables the fleet to avoid external obstacles while keeping the formation. This approach mitigates the issue of vehicles straying out of communication range while evading obstacles. We modify the collision cones method from [12] to be compatible with double integrator dynamics and focus on obstacle avoidance in the xy-plane.

We assume a constant velocity model for the obstacle. Its position and velocity vectors are denoted by $\mathbf{p}_o = [x_o, y_o, z_o]^{\mathrm{T}}$ and $\mathbf{v}_o = [\dot{x}_o, \dot{y}_o, \dot{z}_o]^{\mathrm{T}}$. We define an obstacle avoidance radius r_o that is large enough to account for both the size of the obstacle and the AUV. The formation radius r_f is defined as the maximum distance between any vehicle in the fleet and the formation center, and it is assumed to be constant. We further define $\mathbf{p}_{rel} = [x_b - x_o, y_b - y_o]^{\mathrm{T}}$, $\mathbf{v}_{rel} = [\dot{x}_{LOS,d} - \dot{x}_o, \dot{y}_{LOS,d} - \dot{y}_o]^{\mathrm{T}}$, and $\dot{\mathbf{v}}_{rel} = [\ddot{x}_{LOS,d}, \ddot{y}_{LOS,d}]^{\mathrm{T}}$. Note that $\mathbf{v}_{rel}$ is defined in terms of the LOS velocity (32), so, in general, $\dot{\mathbf{p}}_{rel} \neq \mathbf{v}_{rel}$.

Collision is avoided if we ensure

$$\|\mathbf{p}_{rel}\| \geq r_o + r_f \tag{40}$$

throughout the avoidance maneuver (see Fig. 3(a)). The formation is on a collision course (see Fig. 3(b)), if

$$|\angle(-\mathbf{p}_{rel}, \mathbf{v}_{rel})| \leq \alpha, \quad \alpha = \sin^{-1}\big(\frac{r_o + r_f}{\|\mathbf{p}_{rel}\|}\big). \tag{41}$$

Then the obstacle avoidance task is activated if the fleet is close enough so that $\alpha > \alpha_{\min}$. When the task is active, the x- and y-components of $\mathbf{v}_{LOS,d}$ and $\dot{\mathbf{v}}_{LOS,d}$ given by (32) are replaced with $\mathbf{v}_{OA,d}$ and $\dot{\mathbf{v}}_{OA,d}$, given by

$$\mathbf{v}_{OA,d} = \|\mathbf{v}_{rel}\| \left[\cos(\psi_{OA}), \sin(\psi_{OA})\right]^{\mathrm{T}} + [\dot{x}_o, \dot{y}_o]^{\mathrm{T}}, \tag{42}$$

$$\begin{aligned}\dot{\mathbf{v}}_{OA,d} = &\left(\tfrac{\mathrm{d}}{\mathrm{d}t}\|\mathbf{v}_{rel}\|\right)\left[\cos(\psi_{OA}), \sin(\psi_{OA})\right]^{\mathrm{T}} \\ &+ \|\mathbf{v}_{rel}\|\Big[-\sin(\psi_{OA})\dot{\psi}_{OA}, \cos(\psi_{OA})\dot{\psi}_{OA}\Big]^{\mathrm{T}},\end{aligned} \tag{43}$$

where

$$\psi_{OA} = \operatorname{atan_2}(y_o - y_b, x_o - x_b) \pm \alpha, \tag{44}$$

$$\dot{\psi}_{OA} = \frac{(x_o - x_b)(\dot{y}_o - \dot{y}_b) - (y_o - y_b)(\dot{x}_o - \dot{x}_b)}{\|\mathbf{p}_{rel}\|^2} \pm \dot{\alpha}, \tag{45}$$

$$\dot{\alpha} = \frac{r_o + r_f}{\|\mathbf{p}_{rel}\|^2\sqrt{\|\mathbf{p}_{rel}\|^2 - (r_o + r_f)^2}}\mathbf{p}_{rel}^{\mathrm{T}}\dot{\mathbf{p}}_{rel}, \tag{46}$$

before entering into (31).

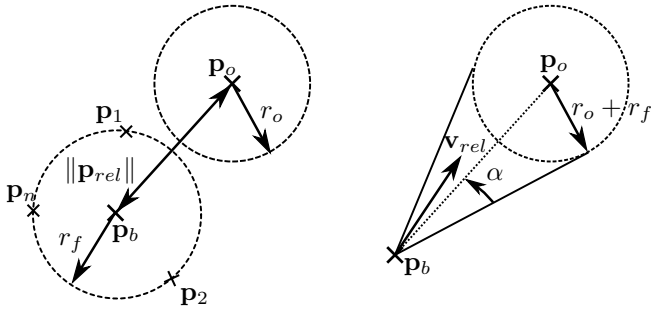

(a) Illustration of the obstacle avoidance constraint (40). (b) Illustration of the conflict condition (41).

Fig. 3. Illustrations of obstacle avoidance.

E. Closed-Loop Analysis

In this section, we analyze the closed-loop stability of the system's external states and the boundedness of the internal states. We assume that the inter-vehicle collision avoidance task is inactive for the analysis. Since the path-following and formation-keeping tasks are orthogonal, the null-space projection $\mathbf{N}_2$ from the formation-keeping task will not affect the path-following acceleration $\mathbf{v}_3$. Consequently, the total acceleration of the vehicles is given by

$$\dot{\mathbf{v}} = \dot{\mathbf{v}}_2 + \dot{\mathbf{v}}_3. \tag{47}$$

Furthermore, because of the following independence relations

$$\ddot{\boldsymbol{\sigma}}_2 = \mathbf{J}_2\dot{\mathbf{v}}_2 + \mathbf{J}_2\dot{\mathbf{v}}_3 = \mathbf{J}_2\dot{\mathbf{v}}_2, \tag{48}$$

$$\dot{\mathbf{v}}_b = \frac{1}{n}\sum_{i=1}^{n}(\dot{\mathbf{v}}_2 + \dot{\mathbf{v}}_3) = \frac{1}{n}\sum_{i=1}^{n}\dot{\mathbf{v}}_3, \tag{49}$$

the closed-loop properties of each task can be analyzed separately.

1) Stability of the Formation-Keeping Task: The closed-loop dynamics of the formation-task error $\tilde{\boldsymbol{\sigma}}_2$ under the saturated formation-keeping acceleration, (28), are given by the system

$$\ddot{\tilde{\boldsymbol{\sigma}}}_2 = -v_{2_{\max}}\mathrm{sat}\big(\boldsymbol{\Lambda}_{p,2}\tilde{\boldsymbol{\sigma}}_2\big) - \boldsymbol{\Lambda}_{d,2}\dot{\tilde{\boldsymbol{\sigma}}}_2. \tag{50}$$

Theorem 2: Let $\boldsymbol{\Lambda}_{p,2}$, $\boldsymbol{\Lambda}_{d,2}$ be two symmetric positive definite matrices so that the product $\boldsymbol{\Lambda}_{p,2}\boldsymbol{\Lambda}_{d,2}$ is symmetric positive definite. Then, $\left[\dot{\tilde{\boldsymbol{\sigma}}}_2^{\mathrm{T}}, \tilde{\boldsymbol{\sigma}}_2^{\mathrm{T}}\right]^{\mathrm{T}} = \mathbf{0}$ is a uniformly globally asymptotically stable (UGAS) equilibrium of the closed-loop system (50).

Proof: Consider the Lyapunov function

$$\begin{aligned}V(\tilde{\boldsymbol{\sigma}}_2, \dot{\tilde{\boldsymbol{\sigma}}}_2) = &\, v_{2,\max}\log\left(\cosh\|\boldsymbol{\Lambda}_{p,2}\tilde{\boldsymbol{\sigma}}_2\|\right) \\ &+ \frac{1}{2}\dot{\tilde{\boldsymbol{\sigma}}}_2^{\mathrm{T}}\boldsymbol{\Lambda}_{p,2}\dot{\tilde{\boldsymbol{\sigma}}}_2.\end{aligned} \tag{51}$$

Inserting for (50), the time-derivative is given by

$$\begin{aligned}\dot{V} = &\, v_{2,\max}\mathrm{sat}\left(\boldsymbol{\Lambda}_{p,2}\tilde{\boldsymbol{\sigma}}_2\right)^{\mathrm{T}}\boldsymbol{\Lambda}_{p,2}\dot{\tilde{\boldsymbol{\sigma}}}_2 \\ &- \dot{\tilde{\boldsymbol{\sigma}}}_2^{\mathrm{T}}\boldsymbol{\Lambda}_{p,2}\left(v_{2,\max}\mathrm{sat}\left(\boldsymbol{\Lambda}_{p,2}\tilde{\boldsymbol{\sigma}}_2\right) + \boldsymbol{\Lambda}_{d,2}\dot{\tilde{\boldsymbol{\sigma}}}_2\right), \\ = &\, -\dot{\tilde{\boldsymbol{\sigma}}}_2^{\mathrm{T}}\boldsymbol{\Lambda}_{p,2}\boldsymbol{\Lambda}_{d,2}\dot{\tilde{\boldsymbol{\sigma}}}_2.\end{aligned} \tag{52}$$

Let $S = \{\left[\dot{\tilde{\boldsymbol{\sigma}}}_2^{\mathrm{T}}, \tilde{\boldsymbol{\sigma}}_2^{\mathrm{T}}\right]^{\mathrm{T}} \in \mathbb{R}^{6(n-1)} | \dot{V} = 0\}$. Because of the dynamics (50), no other solution can stay identically in S, other than the trivial solution $\left[\dot{\tilde{\boldsymbol{\sigma}}}_2^{\mathrm{T}}, \tilde{\boldsymbol{\sigma}}_2^{\mathrm{T}}\right]^{\mathrm{T}} \equiv \mathbf{0}$. Thus, the origin is globally asymptotically stable according to [24, Corollary 4.2]. Furthermore, because (50) is time-invariant, the equilibrium is UGAS. ∎

2) Stability of the Path-Following Task: Let $\tilde{\mathbf{p}}$ and $\tilde{\mathbf{v}}$ be given by (36). Using the definition

$$\mathbf{p}_b^p = \mathbf{R}_p^{\mathrm{T}}(\mathbf{p}_b - \mathbf{p}_p), \tag{53}$$

we get the following error system

$$\begin{aligned} \dot{\tilde{\mathbf{p}}} &= \tilde{\mathbf{v}}, \\ \dot{\tilde{\mathbf{v}}} &= -\boldsymbol{\Lambda}_{p,3}\tilde{\mathbf{v}} - \boldsymbol{\Lambda}_{i,3}\tilde{\mathbf{p}}, \end{aligned} \tag{54a}$$

$$\begin{aligned} \dot{\mathbf{p}}_b^p &= f(\cdot) + g(\cdot)\tilde{\mathbf{v}}, \\ &= \mathbf{R}_p^{\mathrm{T}}(\mathbf{v}_b + \mathbf{v}_c - \dot{\mathbf{p}}_p) + \left(\mathbf{S}(\omega_p\dot{\xi})\right)^{\mathrm{T}}\mathbf{R}_p^{\mathrm{T}}(\mathbf{p}_b - \mathbf{p}_p), \\ &= \mathbf{R}_p^{\mathrm{T}}(\mathbf{v}_{LOS,d} - \dot{\mathbf{p}}_p) - \mathbf{S}(\omega_p\dot{\xi})\mathbf{p}_b^p + \mathbf{R}_p^{\mathrm{T}}\tilde{\mathbf{v}}. \end{aligned} \tag{54b}$$

Theorem 3: Let $\boldsymbol{\Lambda}_{p,3}$, $\boldsymbol{\Lambda}_{i,3}$ be positive definite matrices. Then, $[\tilde{\mathbf{p}}^{\mathrm{T}}, \tilde{\mathbf{v}}^{\mathrm{T}}, (\mathbf{p}_b^p)^{\mathrm{T}}]^{\mathrm{T}} = \mathbf{0}$ is a uniformly semiglobally exponentially stable equilibrium (USGES) of the system (54a)-(54b).

Proof: Note that the error system is in a cascaded form where the velocity error $\tilde{\mathbf{v}}$ from (54a) perturbs the system (54b). The dynamics of the perturbing system (54a) are GES according to Lemma 1. The nominal system (54b) with $\tilde{\mathbf{v}} = \mathbf{0}$ was proved to be USGES in [12] using the Lyapunov function

$$V(\mathbf{p}_b^p) = \frac{1}{2}\left(\mathbf{p}_b^p\right)^{\mathrm{T}}\mathbf{p}_b^p. \tag{55}$$

Therefore, according to [25, Proposition 9] the cascaded system is USGES if the following two assumptions hold

1) There exist constants c_1, c_2, $\eta > 0$ such that

$$\left\|\frac{\partial V}{\partial \mathbf{p}_b^p}\right\| \|\mathbf{p}_b^p\| \leq c_1 V(\mathbf{p}_b^p), \quad \forall \|\mathbf{p}_b^p\| \geq \eta, \tag{56}$$

$$\left\|\frac{\partial V}{\partial \mathbf{p}_b^p}\right\| \leq c_2, \quad \forall \|\mathbf{p}_b^p\| \leq \eta. \tag{57}$$

2) There exist two continuous functions α_1, $\alpha_2 : \mathbb{R}_{\geq 0} \to \mathbb{R}_{\geq 0}$, such that $\mathbf{g}(\cdot)$ satisfies

$$\|g(\cdot)\| \leq \alpha_1(\|\tilde{\mathbf{v}}\|) + \alpha_2(\|\tilde{\mathbf{v}}\|)\|\mathbf{p}_b^p\|. \tag{58}$$

Because $\|\partial V/\partial \mathbf{p}_b^p\| = \|\mathbf{p}_b^p\|$, 1) holds with $c_1 = 2$, $c_2 = \eta$ for any $\eta \in \mathbb{R}_{\geq 0}$.

Equation (58) is satisfied with $\alpha_1(\|\tilde{\mathbf{v}}\|) = 1, \alpha_2(\|\tilde{\mathbf{v}}\|) = 0$, because $\|g(\cdot)\| = \|\mathbf{R}_p^{\mathrm{T}}\| = 1$. As a result, all assumptions of [25, Proposition 9] are satisfied, and the origin of the closed-loop path-following system (54a)-(54b) is USGES. ∎

3) Boundedness of Internal States: The proofs in this section are based on [20]. For brevity, we will omit those derivations that can be directly found in [20].

We note that the only states that can grow unboundedly are the angular velocities of the vehicles. Let p_i, q_i, and r_i denote the roll, pitch, and yaw rate of vehicle i (note that $\boldsymbol{\omega}_i^{\mathrm{T}} = [p_i, q_i, r_i]$). Furthermore, let $\mathbf{p}_{\mathrm{d},i} = \mathbf{p}_p(\xi) + \mathbf{R}_p\mathbf{p}_{f,i}^f$ denote the desired position of vehicle i. Note that because the path function is $\mathcal{C}^\infty$ and thanks to the choice of the path parameter update law (39), the time-derivative of $\mathbf{p}_{\mathrm{d},i}$ is bounded.

First, we investigate the roll rate dynamics. In [20], it is shown that the roll rate dynamics are always bounded. Specifically, there exist $a_x, b_x > 0$ such that

$$|p_i(t)| \leq |p_i(0)|\,\mathrm{e}^{-a_x t} + \frac{b_x}{a_x}\left(1 - \mathrm{e}^{-a_x t}\right). \tag{59}$$

Now, we investigate the pitch and yaw rate dynamics. The closed-loop expression for $\dot{q}_i$ and $\dot{r}_i$ is

$$\begin{aligned} \begin{bmatrix}\dot{q}_i \\ \dot{r}_i\end{bmatrix} = \begin{bmatrix}0 & 0 & -\frac{1}{h} \\ 0 & \frac{1}{h} & 0\end{bmatrix} \Big(&\mathbf{R}_i^{\mathrm{T}}\boldsymbol{\mu}_i + \mathcal{D}_\nu(\boldsymbol{\zeta}_{r,i}) + \mathcal{C}_\nu(\boldsymbol{\zeta}_{r,i}) \\ &- \boldsymbol{\omega}_i \times \mathbf{R}_i^{\mathrm{T}}\mathbf{x}_{2,i}\Big). \end{aligned} \tag{60}$$

Note that under the NSB control law, the hand velocity $\mathbf{x}_{2,i}$ converges to $\dot{\mathbf{p}}_{\mathrm{d},i} - \mathbf{v}_c$. Consider then the following Lyapunov function candidate

$$V_{\omega_i}(q_i, r_i) = \frac{1}{2}\left(q_i^2 + r_i^2\right). \tag{61}$$

In [20], it is shown that the following inequality holds for the time-derivative of V_{ω_i}

$$\begin{aligned} \dot{V}_{\omega_i} \leq &- a_y q_i^2 - a_z r_i^2 + \|\mathbf{x}_{2,i}\|\,\|[q_i, r_i]\|\left(\frac{\|\boldsymbol{\omega}_i\|}{h} + a_e\right) \\ &+ a_{xyz} p_i q_i r_i + a_{xy}\|\mathbf{x}_{2,i}\|\,p_i q_i + a_{xz}\|\mathbf{x}_{2,i}\|\,p_i r_i \\ &+ a_{ye}\|\mathbf{x}_{2,i}\|\,q_i^2 + a_{ze}\|\mathbf{x}_{2,i}\|\,r_i^2 + a_{ey}\|\mathbf{x}_{2,i}\|^2 q_i \\ &+ a_{ez}\|\mathbf{x}_{2,i}\|^2 q_i + \|[q_i, r_i]\|\,\|\boldsymbol{\mu}_i\|. \end{aligned} \tag{62}$$

Theorem 4: Let us define

$$\bar{p} = b_x/a_x, \qquad \bar{\mathbf{x}}_2 = \max_{t \in \mathbb{R}_{\geq 0}} \|\dot{\mathbf{p}}_{\mathrm{d},i}(t) - \mathbf{v}_c\|, \tag{63a}$$

$$\bar{\alpha}_y = a_y - \left(\frac{1}{h}\bar{\mathbf{x}}_2 + \frac{1}{2}|a_{xyz}\bar{p}| + |a_{ye}\bar{\mathbf{x}}_2|\right), \tag{63b}$$

$$\bar{\alpha}_z = a_z - \left(\frac{1}{h}\bar{\mathbf{x}}_2 + \frac{1}{2}|a_{xyz}\bar{p}| + |a_{ze}\bar{\mathbf{x}}_2|\right). \tag{63c}$$

The angular rate dynamics are ultimately bounded if $a_x, \bar{\alpha}_y, \bar{\alpha}_z > 0$.

Proof: Using the identities described in [20], we can derive the following (looser) upper bound on $\dot{V}_{\omega_i}$

$$\dot{V}_{\omega_i} \leq -\alpha_y q_i^2 - \alpha_z r_i^2 + G\left(\mathbf{x}_{2,i}, \boldsymbol{\omega}_i, \boldsymbol{\mu}_i\right), \tag{64}$$

where

$$\alpha_y = \left(a_y - \left(\frac{1}{h}\|\mathbf{x}_2\| + \frac{1}{2}|a_{xyz}||p_i| + |a_{ye}|\,\|\mathbf{x}_2\|\right)\right), \tag{65a}$$

$$\alpha_z = \left(a_z - \left(\frac{1}{h}\|\mathbf{x}_2\| + \frac{1}{2}|a_{xyz}||p_i| + |a_{ze}|\,\|\mathbf{x}_2\|\right)\right), \tag{65b}$$

and $G(\cdot)$ represents the terms that grow at most linearly with q_i and r_i. Note that the two following limits

$$\lim_{t\to\infty} \alpha_y \geq \bar{\alpha}_y, \qquad \lim_{t\to\infty} \alpha_z \geq \bar{\alpha}_z, \tag{66}$$

hold for α_y and α_z. Therefore, if $\bar{\alpha}_y, \bar{\alpha}_z > 0$, then there

exists a finite time T after which $\alpha_y, \alpha_z > 0$.

First, let us investigate the candidate Lyapunov function for $t < T$. Since α_y and α_z may be negative, we cannot prove boundedness. However, note that the derivative of the Lyapunov function in (64) has the following form

$$\dot{V}_{\boldsymbol{\omega}_i} \leq k \left\| \widehat{\boldsymbol{\omega}}_i \right\|^2 + G(\cdot), \tag{67}$$

where $\widehat{\boldsymbol{\omega}}_i := [q_i, r_i]^{\mathrm{T}}$, k is a positive constant, and $G(\cdot)$ grows at most linearly with $\|\widehat{\boldsymbol{\omega}}_i\|$. We can therefore conclude that the dynamics of q_i and r_i are forward complete [26].

For $t \geq T$, $\dot{V}_{\boldsymbol{\omega}_i}$ has the following form

$$\dot{V}_{\omega_i} \leq -\alpha_y q_i^2 - \alpha_z r_i^2 + G(\cdot) \tag{68}$$

For sufficiently large angular velocities, the quadratic term will dominate the linear term $G(\cdot)$, and q and r will remain bounded.

The angular rate dynamics are thus ultimately bounded. ■

F. Simulation results

To validate the theoretical results, we perform a simulation where the proposed algorithm is applied to a fleet of three LAUVs [27]. In the simulated scenario, the vehicles should follow a continuous, differentiable spiral while avoiding collision with a stationary cylindrical-shaped obstacle with radius $10\,\mathrm{m}$, base circle in the xy-plane and origin $[x, y] = [100, -10]$. All position variables are here given in meters. The spiral path is given by

$$\mathbf{p}_p(\xi) = \mathbf{p}_{p,0} + \left[\xi, -40\cos(\tfrac{\pi}{100}\xi), 20\sin(\tfrac{\pi}{100}\xi)\right]^{\mathrm{T}}, \tag{69}$$

where

$$\mathbf{p}_{p,0} = \left[0, -40, 35\right]^{\mathrm{T}}. \tag{70}$$

The barycenter relative formation is given by

$$\mathbf{p}_{f,1}^f = \begin{bmatrix} 0 \\ 10 \\ 5 \end{bmatrix}, \quad \mathbf{p}_{f,1}^f = \begin{bmatrix} 0 \\ -10 \\ 5 \end{bmatrix}, \quad \mathbf{p}_{f,1}^f = \begin{bmatrix} 0 \\ 0 \\ -10 \end{bmatrix}, \tag{71}$$

and we want the collision avoidance task to ensure a safe distance of $10\,\mathrm{m}$ both between vehicles in the fleet and external obstacles. Therefore, the avoidance radius of the cylinder, $\mathbf{r}_o$, is $20\,\mathrm{m}$. The vehicles are subject to an unknown ocean current

$$\mathbf{v}_c = \begin{bmatrix} 0 & 0.25 & 0.05 \end{bmatrix}^{\mathrm{T}}\ \mathrm{m/s}. \tag{72}$$

The initial position of the barycenter is $\mathbf{p}_b = [-5, -100, 18]^{\mathrm{T}}$ and the relative positions are

$$\boldsymbol{\sigma}_{2,1} = \begin{bmatrix} 0 \\ -15 \\ -7 \end{bmatrix}, \quad \boldsymbol{\sigma}_{2,2} = \begin{bmatrix} 0 \\ 15 \\ -7 \end{bmatrix}, \quad \boldsymbol{\sigma}_{2,3} = \begin{bmatrix} 0 \\ 0 \\ 14 \end{bmatrix}. \tag{73}$$

The resulting North-East trajectory of the mission is shown in Figure 5. The vehicles avoid the obstacle with a margin and return to the desired path. Figure 4(a) shows that the angular velocities remain bounded, in accordance with Theorem 4. Figure 4(b) shows that the fleet converges to the desired formation while the obstacle avoidance mode is active. Except for during the inter-vehicle collision avoidance, the convergence seems linear, which can be expected because the task velocity is saturated by $v_{2,\max}$. Figure 4(c) shows that the inter-vehicle COLAV task activates when the distance between vehicles is below d_{COLAV}, and the distance does not decrease further. Because the obstacle avoidance radius r_o was chosen $10\mathrm{m}$ wider than the obstacle, the obstacle is avoided with a $10\mathrm{m}$ margin. Figure 4(d) shows that the path-following error initially increases as the fleet avoids the obstacle because the x- and y-components of $\mathbf{v}_{LOS,d}$ and $\dot{\mathbf{v}}_{LOS,d}$ are replaced with $\mathbf{v}_{OA,d}$ and $\dot{\mathbf{v}}_{OA,d}$ given by (42), (43). As expected from Theorem 3, the error converges to zero after the obstacle is passed when the LOS task is activated again.

IV. Conclusions and future work

In this paper, we proposed an extended NSB method for double-integrator systems. The dynamics of the vehicles are controlled directly in task space such that the closed-loop behaviors of the tasks can be interpreted as mass-spring-damper-systems. Consequently, the control gains can be chosen such that the closed-loop system is critically damped. The method was proved to render the task error dynamics globally exponentially stable. The method was then demonstrated in a case study of formation path following with underactuated AUVs. We defined the second-order kinematic tasks for collision avoidance, formation keeping, and path following. To force a bounded velocity, we introduced a saturation term to the formation-keeping acceleration. The closed-loop formation-error system with the reformulated formation-keeping acceleration was proved to be UGAS. The closed-loop path-following system was proved to be USGES. Simulation results demonstrate the effectiveness of our approach. Possible future work includes verifying the presented results through experiments.

References

[1] M. Soorki, H. Talebi, and S. Nikravesh, "A robust dynamic leader-follower formation control with active obstacle avoidance," in *Proc. 2011 IEEE International Conference on Systems, Man, and Cybernetics*, Oct. 2011, pp. 1932–1937.

[2] R. Cui, S. Sam Ge, B. Voon Ee How, and Y. Sang Choo, "Leader–follower formation control of underactuated autonomous underwater vehicles," *Ocean Engineering*, vol. 37, Dec. 2010.

[3] Y. Wang, W. Yan, and W. Yan, "A leader-follower formation control strategy for AUVs based on line-of-sight guidance," in *Proc. 2009 International Conference on Mechatronics and Automation*, Aug. 2009, pp. 4863–4867.

[4] R. Skjetne, S. Moi, and T. Fossen, "Nonlinear formation control of marine craft," in *Proc. 41st IEEE Conference on Decision and Control*, Dec. 2002, pp. 1699–1704.

[5] R. Ghabcheloo, A. P. Aguiar, A. Pascoal, C. Silvestre, I. Kaminer, and J. Hespanha, "Coordinated path-following control of multiple underactuated autonomous vehicles in the presence of communication failures," in *Proc. 45th IEEE Conference on Decision and Control*, Dec. 2006, pp. 4345–4350.

[6] E. Borhaug and K. Y. Pettersen, "Formation control of 6-DOF Euler-Lagrange systems with restricted inter-vehicle communication," in *Proc. 45th IEEE Conference on Decision and Control*, Dec. 2006.

[7] S. Monteiro and E. Bicho, "A dynamical systems approach to behavior-based formation control," in *Proc. 2002 IEEE International Conference on Robotics and Automation*, May 2002, pp. 2606–2611.

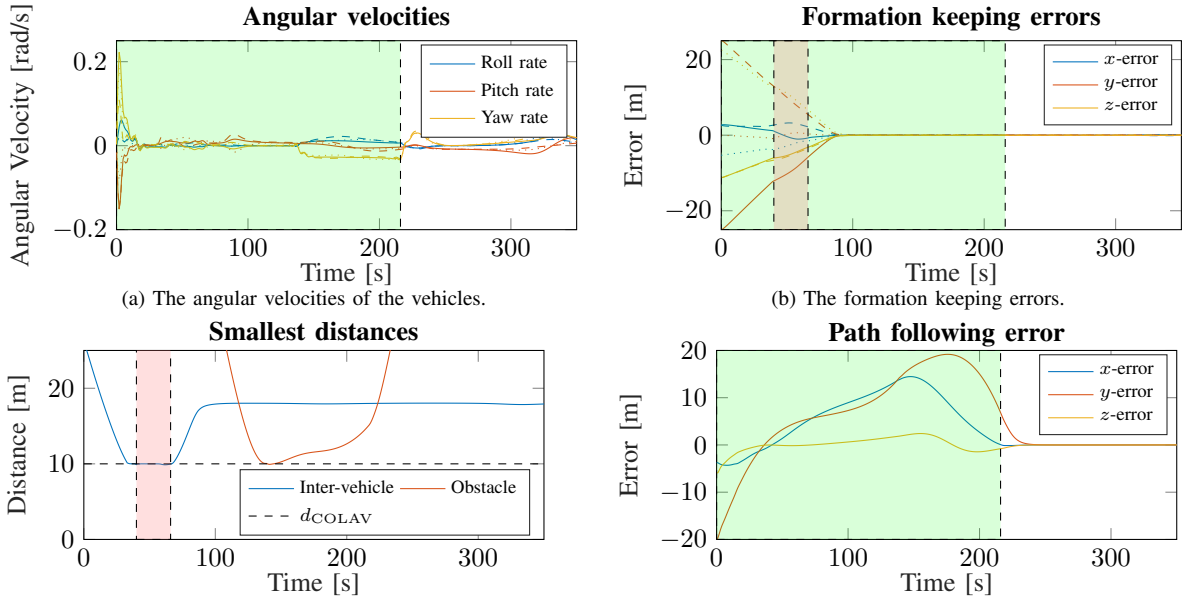

(a) The angular velocities of the vehicles.

(b) The formation keeping errors.

(c) The minimum inter-vehicle and obstacle distance.

(d) The path-following error of the barycenter.

Fig. 4. Simulation results of the path-following algorithm proposed in Section III. The full, dashed, and dotted lines correspond to the three different vehicles. The green and red rectangles represent when obstacle avoidance and inter-vehicle COLAV is active.

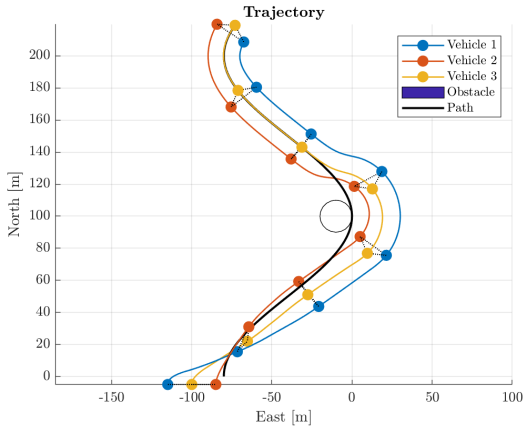

Fig. 5. The trajectory of the vehicles. The markers represent the vehicle positions every 50 seconds.

[8] T. Balch and R. Arkin, "Behavior-based formation control for multirobot teams," *IEEE Transactions on Robotics and Automation*, vol. 14, no. 6, pp. 926–939, Dec. 1998.

[9] B. Das, B. Subudhi, and B. B. Pati, "Cooperative formation control of autonomous underwater vehicles: An overview," *International Journal of Automation and Computing*, vol. 13, no. 3, pp. 199–225, Jun. 2016.

[10] F. Arrichiello, S. Chiaverini, and T. I. Fossen, "Formation control of underactuated surface vessels using the null-space-based behavioral control," in *Proc. 2006 IEEE/RSJ International Conference on Intelligent Robots and Systems*, Oct. 2006, pp. 5942–5947.

[11] Å. Eek, K. Y. Pettersen, E.-L. M. Ruud, and T. R. Krogstad, "Formation path following control of underactuated USVs," *European Journal of Control*, vol. 62, pp. 171–184, Nov. 2021.

[12] J. Matouš, K. Y. Pettersen, D. Varagnolo, and C. Paliotta, "Singularity-free formation path following of underactuated AUVs," in *Proc. 22nd IFAC World Congress*, Jul. 2023.

[13] F. Arrichiello, H. Heidarsson, S. Chiaverini, and G. S. Sukhatme, "Cooperative caging using autonomous aquatic surface vehicles," in *Proc. 2010 IEEE International Conference on Robotics and Automation*, May 2010, pp. 4763–4769.

[14] F. J. Pereda, H. G. de Marina, J. M. Giron-Sierra, and J. Jimenez, "Towards automatic oil spill confinement with autonomous marine surface vehicles," in *Proc. OCEANS 2011*, Jun. 2011.

[15] B. Siciliano, L. Sciavicco, L. Villani, and G. Oriolo, "Differential Kinematics and Statics," in *Robotics: Modelling, Planning and Control*, ser. Advanced Textbooks in Control and Signal Processing. London: Springer, 2009, pp. 105–160.

[16] S. Chiaverini, G. Oriolo, and I. D. Walker, "Kinematically Redundant Manipulators," in *Springer Handbook of Robotics*, B. Siciliano and O. Khatib, Eds. Berlin, Heidelberg: Springer, 2008, pp. 245–268.

[17] E. Restrepo, J. Matouš, and K. Y. Pettersen, "Tracking-in-formation of multiple autonomous marine vehicles under proximity and collision-avoidance constraints," in *Proc. 2022 European Control Conference*, Jul. 2022, pp. 930–937.

[18] X. Cai and M. d. Queiroz, "Adaptive rigidity-based formation control for multirobotic vehicles with dynamics," *IEEE Transactions on Control Systems Technology*, vol. 23, no. 1, pp. 389–396, Jan. 2015.

[19] C. Paliotta, E. Lefeber, K. Y. Pettersen, J. Pinto, M. Costa, and J. T. de Figueiredo Borges de Sousa, "Trajectory tracking and path following for underactuated marine vehicles," *IEEE Transactions on Control Systems Technology*, vol. 27, no. 4, pp. 1423–1437, Jul. 2019.

[20] J. Matouš, C. Paliotta, K. Y. Pettersen, and D. Varagnolo, "Trajectory tracking and path following of underactuated AUVs using the hand position concept," *Submitted to IEEE Transactions on Control Systems Technology*, 2023, preprint available at https://www.dropbox.com/s/pwyople7rpykge9/SubmittedVersion.pdf?dl=0.

[21] G. Antonelli and S. Chiaverini, "Kinematic control of platoons of autonomous vehicles," *IEEE Transactions on Robotics*, vol. 22, no. 6, pp. 1285–1292, Dec. 2006.

[22] B. Siciliano, "A closed-loop inverse kinematic scheme for on-line joint-based robot control," *Robotica*, vol. 8, no. 3, p. 231–243, 1990.

[23] G. Antonelli, F. Arrichiello, and S. Chiaverini, "Stability analysis for the null-space-based behavioral control for multi-robot systems," in *Proc. 47th IEEE Conference on Decision and Control*, 2008.

[24] H. K. Khalil, *Nonlinear Systems*. Prentice Hall, 2002.

[25] K. Y. Pettersen, "Lyapunov sufficient conditions for uniform semiglobal exponential stability," *Automatica*, vol. 78, Apr. 2017.

[26] D. Angeli and E. D. Sontag, "Forward completeness, unboundedness observability, and their Lyapunov characterizations," *Systems & Control Letters*, vol. 38, no. 4, pp. 209–217, Dec. 1999.

[27] A. Sousa, L. Madureira, J. Coelho, J. Pinto, J. Pereira, J. Borges Sousa, and P. Dias, "LAUV: The man-portable autonomous underwater vehicle," *IFAC Proceedings Volumes*, vol. 45, no. 5, Jan. 2012.